arXiv:2005.07982v1 [quant-ph] 16 May 2020

Article

Counting of Hong-Ou-Mandel Bunched Optical Photons Using a Fast Pixel Camera

Andrei Nomerotski [1]*, Michael Keach [1], Paul Stankus [1], Peter Svihra [2,3] and Stephen Vintskevich[4]

[1] Brookhaven National Laboratory, Upton NY 11973, USA
[2] Department of Physics, Faculty of Nuclear Sciences and Physical Engineering, Czech Technical University, Prague 115 19, Czech Republic
[3] Department of Physics and Astronomy, School of Natural Sciences, University of Manchester, Manchester M13 9PL, United Kingdom
[4] Moscow Institute of Physics and Technology, Institutskii Per. 9, Dolgoprudny, Moscow Region 141700, Russia
* Correspondence: anomerotski@bnl.gov

Version March 14, 2024 submitted to Preprints

1. Introduction

Single photons are essential carriers of quantum information, which can be produced, manipulated, and also can travel long distances preserving their quantum state. They are the main constituents of quantum networking protocols, and will likely play a major role in the development of quantum information science (QIS) together with capabilities to process them. The complexity of single photon processing is growing so the photon imaging capabilities, which give access to multi-dimensional information and enable scaling opportunities, are becoming even more important.

Testing a technology for detecting single photons would ideally involve sources to produce single photons, by which we mean modes, either free-space or in fiber waveguides, with a single excitation present deterministically at a known time. Frequently discussed single-photon sources include quantum dots [1], beams of single excited atoms [2,3], readable quantum memories [4–6] and quantum metrology [7]. An alternative approach is to generate tightly time-correlated pairs of photons, where the presence of a "signal" photon is *heralded* by the simultaneous presence of its partner "idler" photon [8,9]

In this work we use a quantum interference effect between two near-simultaneous photons to herald the presence of the pair, and then show that the two photons can be individually detected in both the cases when they are in separate modes and when bunched together in the same mode. Specifically, we combine the near-simultaneous photons through a beam splitter and observe the Hong-Ou-Mandel (HOM) effect [10], which is illustrated schematically in Figure 1

We produce correlated, near-simultaneous pairs of photons through spontaneous parametric down-conversion (SPDC) in a non-linear crystal; these are then coupled in to a fiber-optic beam splitter with a variable delay on one input leg of the beam splitter. The outputs from the single-mode fibers are focused on to a silicon pixel array camera, where we are able to detect both types of outcomes (i) when the photons emerge from different beam splitter output fibers and are detected individually; as well as (ii) when the HOM interference causes both photons to emerge from the same fiber, and here we can detect both members of the pair separately in the pixel camera even while they are in the same spatial mode.

The remainder of the paper is organized as follows. In Section 2 we review different technologies for single photon detection, and in Section 3 we describe the idea of single photon counting using a fast camera with excellent spatial and temporal resolution. Section 4 and Section 5 describe the experimental setup, measurements and data analysis. Section 8 discusses the results and the conclusions that can be drawn.

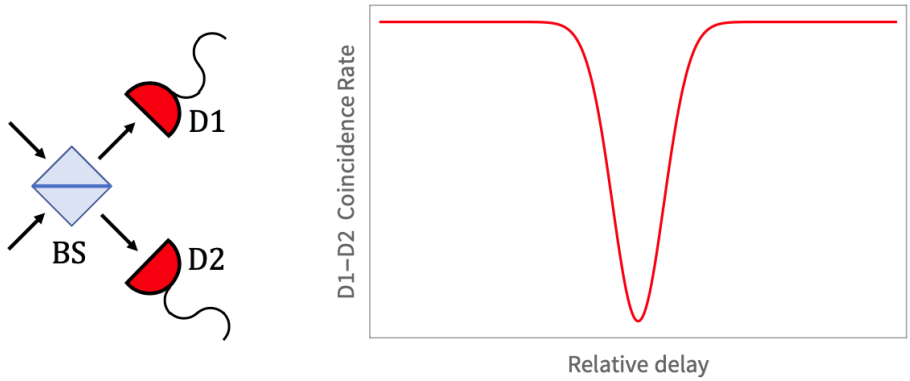


Figure 1. Schematic illustration of the Hong-Ou-Mandel (HOM) effect. *Left:* Two near-simultaneous photons with similar wavelength impinge on a beam splitter (BS), and the outputs are registered on two detectors, D1 and D2. When the photons' arrival is simultaneous, making them indistinguishable, the HOM interference effect causes both photons to exit one side of the splitter or the other, inhibiting the outcome with one photon going to each detector. *Right:* The signature of the HOM effect is a drop in the rate of coincident detections at D1 and D2, as the photon arrival times become identical. This is typically observed as an "HOM dip" in coincidences as a function of some relative time delay at the BS input.

2. Single-photon counting detectors

Quantum applications are one of the major drivers of single photon detection technology, which imposes stringent requirements on their performance in spectral response, quantum efficiency, noise, dead time and time resolution. In general, the capabilities of scientific imaging had spectacular improvements during the last decade with sensitivity, complexity, spatial and time resolution all reaching values unimaginable before. Silicon-based devices remain front-runners in this competition, aided by the consumer-fueled semiconductor industry. Despite this, currently it is not feasible yet to detect a single optical photon with good time resolution in a silicon sensor without prior amplification because of the noise. The amplification can be achieved outside of the sensor using an image intensifier or, alternatively, inside the sensor. In the following we will briefly review possible approaches to single photon counting and will explain where our technique fits. More comprehensive reviews of single photon detection are readily available elsewhere [11–13].

Modern sensors with internal amplification are based on technologies such as electron-multiplying charge coupled devices (EMCCD) and, more recently, single photon avalanche devices (SPAD). In the former the amplification is happening in the additional register in the sensor and the single photon sensitivity can be achieved without compromising the high quantum efficiency of silicon in the range of 400 - 900 nm [14–16]. However the slow frame rate and, therefore, poor time resolution remains a severe limitation for all types of CCDs. SPAD detectors rely on the avalanche breakdown in the diode junction which results in a large pulse of standard amplitude [17–19]. For SPAD designs various architectures are possible, some integrating multiple cells into a single large area device with photon counting capabilities [20] and some using individual SPAD cells. In the latter case the advances in the complementary metal-oxide-semiconductor (CMOS) technology are enabling integration of these devices into pixelated sensors. This led to production of SPAD arrays capable of counting and time stamping single photons with resolution below 100 ps [17,21]. Dark count rate, crosstalk, moderate fill factor (and, hence, reduced detection efficiency) and challenges of integration into a standard CMOS process remain as difficulties of this approach, though the technology is rapidly improving.

Image intensifiers are widely used to convert silicon based CCD and CMOS cameras to high quality single photon imagers. In this case the quantum efficiency is determined by the intensifier photocathode and is limited to about 35%. Traditional CCD and CMOS architectures suffer from the low frame rate. They can efficiently integrate the photon flux in each frame but have limited ability to provide information on photon by photon basis [22–25]. The intensified cameras allow for nanosecond scale time resolution for single photons by gating the image intensifier at expense of low duty cycle since only one gate per frame would be allowed to record the photon by photon information[26]. Photon statistics can be enhanced by using multiple triggers during a single frame, so the camera integrates multiple photons within a single acquired image, but in this case the photon by photon information is lost [27]. Unlike CCDs, the CMOS devices can have more flexible front-end architectures and readout schemes. For example, data-driven designs, which require the signal to cross a threshold for the readout, are well suited for low occupancy, which is common for the single photon applications and allow implementation of complex operations inside the pixels, such as time stamping [28]. In our work here we focus on these devices, which we believe are a promising venue for the QIS applications.

Low temperature sensors, such as superconducting nanowire single photon detectors (SNSPD) [29–31] and transition edge sensors (TES) [32,33], have low energy per produced charge carrier and, hence, have excellent quantum efficiency, including in the infrared telecom range, and amplitude resolution. However, at the same time they have low scalability due to complexity and low-temperature operation.

Counting of single photons is required in multiple applications of QIS, such as advanced photonic quantum computing and quantum key distribution protocols, and for characterization of single photon sources [34,35]. Typically the sources are coupled to fibers so the photons can be sent over considerable distances. Some types of cryogenic sensors, such as TES, have good amplitude resolution and can resolve multiple photons relying on the total signal amplitude. Alternative counting schemes rely on various types of multiplexing when multiple photons are spread over separate devices, either spatially or temporally, and the output is summed [11,20,29]. In the following we demonstrate that counting of photons from a single-mode fiber can be performed using a novel single photon sensitive camera with nanosecond timing resolution, Tpx3Cam. In the context of the above discussion this technique can be considered as a further development of the multiplexing approach taken to the next level with help of modern CMOS technology.

3. Counting of bunched single photons in a fast camera

The idea of counting photons from a fiber by their detection in a position sensitive sensor is illustrated in Figure 2, which shows two simultaneous photons coming out of a fiber and focused on to a pixelated sensor. If the photons are spread enough not to overlap in the sensor they can be detected as separate hits and counted as independent events. Of course, from time to time two photons could coincidentally overlap both in space and time and be counted as a single photon, resulting in inefficiency. So the photon footprint in the sensor, the size of the illuminated spot, pixel deadtime and time resolution all would play roles in the performance of the technique. In the following we present a practical implementation of this approach employing a fast camera and a methodology to characterise it.

The Tpx3Cam camera has superior parameters to enable this technique and can resolve photons spatially and temporally, allowing the photon counting as described above. In our study we used the two-photon Hong-Ou-Mandel (HOM) interference effect to characterize the performance of the photon counting. As illustrated in Fig. 1 the HOM effect will cause two identical photons arriving at a beam splitter to be bunched and exit the splitter on the same side, preventing a coincidence between detections on the two different output fibers. If the photons are completely or partially indistinguishable, for example, if they arrive at the beam splitter not at the same time or, more precisely, if both photons are in orthogonal modes, they could exit on the opposite sides and produce a coincidence between the two fibers. Thus the

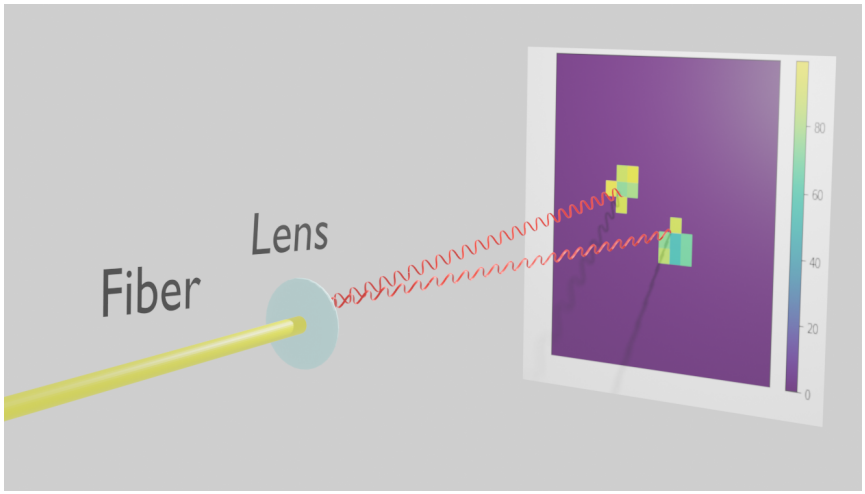


Figure 2. Two photons coming out of a single-mode fiber, focused on to the fast pixel camera and registered individually.

HOM effect allows the production of well-defined states with single and double photons propagating in a fiber if we can control their path lengths and detect their arrivals with sufficient time resolution.

3.1. Tpx3Cam fast camera

Registration of single photons and characterization of the sources in the experiments was performed using an intensified time stamping camera with single photon sensitivity, Tpx3Cam [36,37]. The camera is a hybrid pixel detector: an optical sensor with high quantum efficiency [38] is bump-bonded to Timepix3 [39], a time-stamping readout chip with 256x256 pixels of 55x55 μm^2. The processing electronics in each pixel records the time of arrival (ToA) of hits that cross a preset threshold with 1.6 ns resolution and stores it as time code in a memory inside the pixel. The information about time-over-threshold (ToT), which is related to the deposited energy in each pixel, is also stored. The readout is data driven with pixel dead time of only 475 ns + ToT, which allows multi-hit functionality at the pixel level and fast, 80 Mpix/sec, throughput.

The camera was calibrated to equalize the response of all pixels by adjusting the individual pixel thresholds. After this procedure, the effective threshold to fast light flashes from the intensifier is $600 - 800$ photons per pixel, depending on the wavelength. A small ($\approx 0.1\%$) number of hot pixels was masked to prevent recording large amount of noise hits.

In the single photon sensitive operation, the camera is coupled to a cricket with an intensifier and relay optics to project the light flashes from the intensifier output screen directly on to the optical sensor in the camera. The image intensifier is a vacuum device with a photocathode followed with a micro-channel plate (MCP) and fast scintillator P47. The quantum efficiency (QE) of the GaAs photocathode in the intensifier (Photonis) is about 30% at 810 nm. The MCP efficiency in the used intensifier is close to 100%. A second intensifier with a hi-QE green photocathode was used in series after the first intensifier to ensure efficient detection of the hits. The gains of the both intensifiers were optimised to provide the maximum photon detection efficiency while avoiding saturation. Similar configurations of the intensified Tpx3Cam were used before for characterization of quantum networks [40,41], quantum target detection [42] and lifetime imaging [43] studies.

4. Experimental Setup

Figure 3 shows the experimental setup. The photon pairs are produced in a spontaneous parametric down-conversion (SPDC) source and are sent to a two-to-two fiber-coupled beam splitter with adjustable delay in one of the paths. The output fibers are focused on to the fast camera.

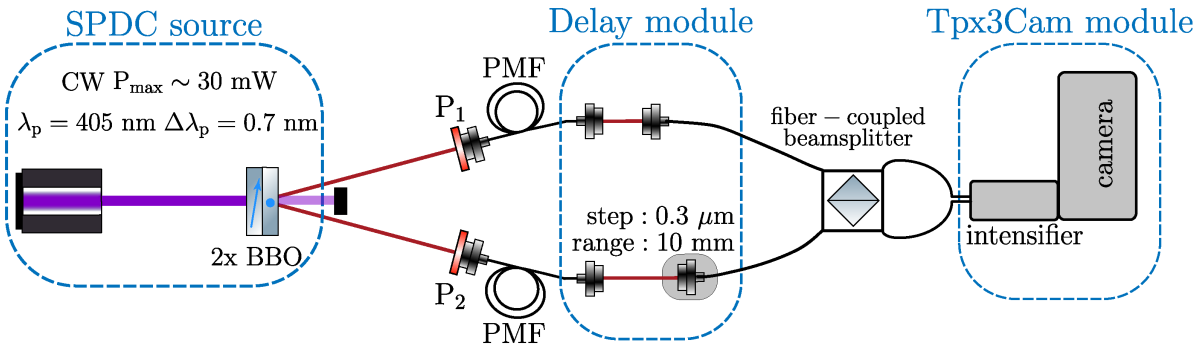


Figure 3. The sketch of the experimental setup. Pump beam produced by continuous-wave (CW) narrow-band ($\Delta\lambda_p \approx 0.7$ nm) laser tuned to the wavelength of ($\lambda_p = 405$nm) (SPDC source). The created SPDC photons are coupled to polarization-maintaining fibers (PMF), where input polarization of photons in both arms is controlled by polarization plates $P_{1,2}$. In the delay module, one can tune an optical path difference between the two legs using a motorized translation stage with 0.3 μm minimal step and dynamic range of 10 mm. Photon counts are recorded with the intensified Tpx3Cam fast camera.

The SPDC source (QuTools QuED)utilizes a blue pump laser diode tuned to the wavelength of 405nm, and a pair of Type I non-collinear BBO crystals with optical axes perpendicular to one another to generate signal and idler photons entangled in polarization at a wavelength of 810 nm. The first crystal optical axis and the pump beam define the vertical plane, so an incoming photon which is vertically polarized gets down-converted and produces two horizontally polarized photons in the first crystal. In contrast, a horizontally polarized photon produces two vertically polarized photons. Signal and idler photons are spatially separated and collected using single-mode fibers. The rate of entangled photon pairs from the source after the fibers was about 10kHz. We used the same source and the camera to spatially characterize photonic polarization entanglement of the SPDC photon source mentioned above [40] so the setup had linear polarizers used for projective measurements. In our experiments the both polarizers were set to 0 degrees, ie vertical polarization, and so only the vertical-vertical branch of the two-photon wave-function survives.

The photons are then coupled into polarization conserving fibers, which keeps them in well-defined modes going into the HOM part of the experiment. Before entering the beam splitter one of the optical paths has an adjustable delay implemented using a step-motor with a minimal step of 0.3 micron and dynamic range of 10 mm. The second optical path is fixed. Main components of the HOM interferometer are shown in a photograph of the optical delay and a fiber-coupled beam splitter in Figure 4. After the splitter the fibers follow to the intensified Tpx3Cam in a dark box and are focused on to the input window of the intensifier shown in the same Figure 4.

5. Data analysis

The data was taken continuously for 20 minutes while slowly scanning the optical delay by changing the distance between the fibers in the 0.3 mm range. Two datasets were acquired, one with the delay scan in one direction and the other one in the opposite direction. The integrated photon counting rate is shown

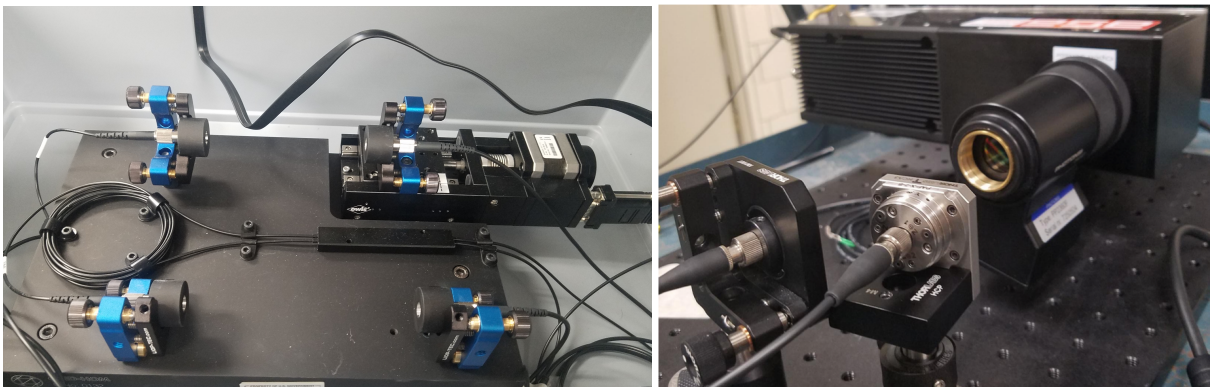


Figure 4. *Left:* photograph of the HOM interferometer with optical delay and beam splitter. *Right:* photograph of Tpx3Cam with two fibers pointing to the intensifier photocathode.

in Figure 5, the two graphs correspond to two fibers. It is visible that the left fiber has a better focusing (narrower width) than the other one.

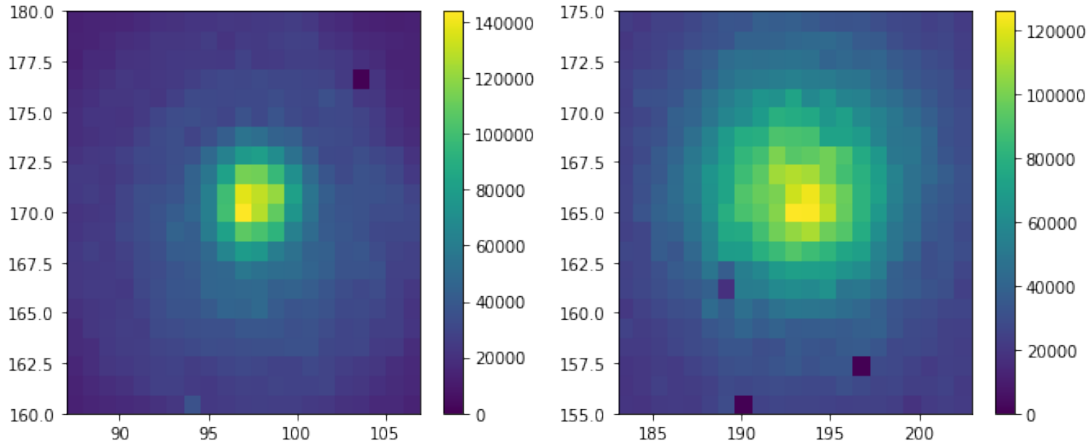


Figure 5. Two-dimensional distribution of pixel occupancy for the two fibers.

After time-ordering, the pixels are combined into the "clusters" using a simple recursive algorithm [37]. Clusters are groups of pixels adjacent to each other and within a preset time window. Each pixel in a cluster should have a neighboring pixel separated not more than 300 ns. Figure 6 shows distribution of number of pixels in the cluster. The average number of pixels per cluster is 9 while there is also an increased number of clusters with four hit pixels due to the symmetry of the 2×2 pixel clusters. The right part of Figure 6 shows the ToT distribution for the brightest pixel in the cluster.

Since all fired pixels measure ToA and ToT independently and have position information, it can be used for centroiding to determine the photon coordinates. The ToT information is used as a weighting factor, yielding an estimate of the coordinates x, y of the incoming single photon. The arrival time of the photon is estimated by using ToA of the pixel with the largest ToT in the cluster. The above ToA is then corrected for the time-walk, an effect caused by the dependence of the pixel electronics time response on the amplitude of the input signal [37,44] achieving 2 ns timing resolution (rms) [37,45].

To identify pairs of simultaneous photons going to the two fibers, we selected areas of the sensor corresponding to regions illuminated by the fibers. The two regions are shown in Figure 5. Then, for each photon detected in one region, we looked for its associated pair at the closest time in the second

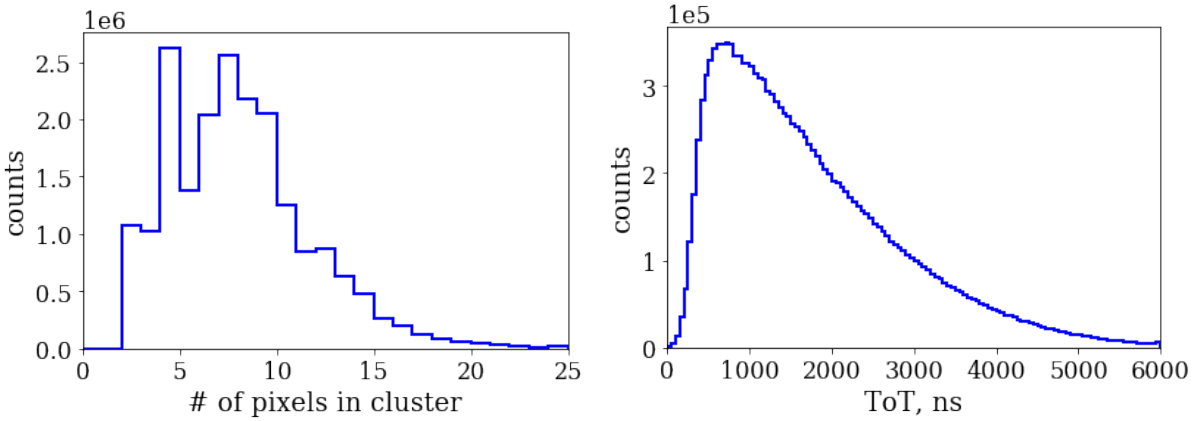


Figure 6. *Left:* distribution of number of pixels in the cluster. *Right:* distribution of time-over-threshold (ToT) for the brightest pixel in the cluster, in ns, corresponding to the pixel intensity.

region. Distribution of time difference of the two photons has a prominent peak at 0 corresponding to the simultaneous photon pairs from the source as shown in the left part of Figure 7. The distribution was fit to a function consisting of two Gaussians and a constant, the latter accounting for flat background of random coincidences. The random coincidences could originate from the coincidences of two background (dark count rate, DCR) photons and also from coincidences of one signal photon and a random photon when the second photon from the same pair is lost due to the photon detection inefficiency. The second photon can be either a DCR photon or a photon from another signal pair. The reconstructed number of signal pairs shown in Figure 7 is 82390 ± 450 and the Gaussian sigma is equal to 7.3 ns for 75% and 17.8 ns for remaining 25% of events in the peak. The statistics is integrated over the whole range of optical delay and represents one of two 20 min datasets.

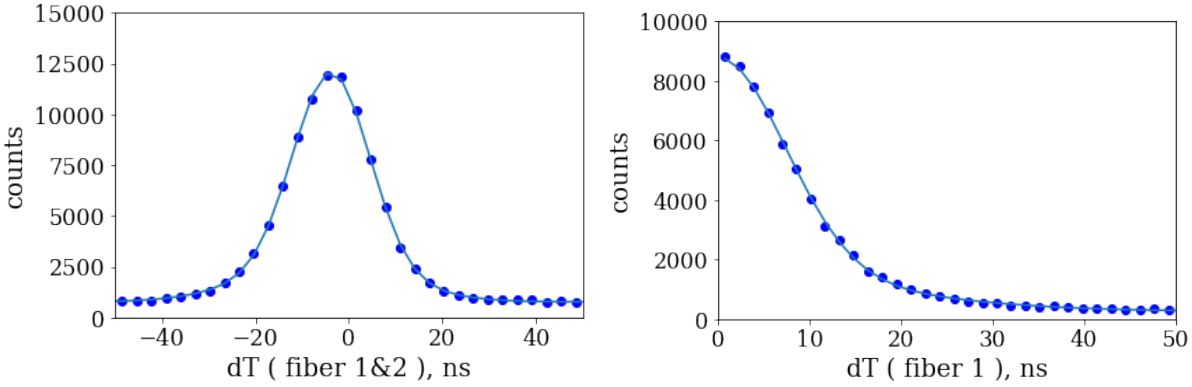


Figure 7. *Left:* distribution of measured time difference between photons registered in fiber 1 and fiber 2. *Right:* distribution of measured time difference between two photons in fiber 1. The distributions are fit with a double Gaussian function and a constant, see the text for detail.

A similar algorithm was used to look for two photons in coincidence exiting the same fiber. In this case the photons from the same fiber were were time ordered so the time difference between them is always positive. The right part of Figure 7 shows the time difference distribution for two photons registered in the same fiber. As in the previous case, there is a prominent peak at 0 indicating strong temporal correlation of the photon pairs. The total number of photon pairs reconstructed in the two fibers is respectively 58370 ± 340 and 58460 ± 370 for the shown dataset. We used the same fit function to determine the number

of events in the peaks and the resulting fit parameters were consistent with the previous fit for two fibers within uncertainties.

Figure 8 shows six examples of two clusters in a single fiber (fiber 2) separated by less than 100 ns. The hits are shown as boxed pairs of heatmaps in ToT representation (left graph in the boxed pair of graphs) and ToA representation (right graph). One can see that the photons could be separated by considerable distances and indeed appear as two independent photons registered by the sensor.

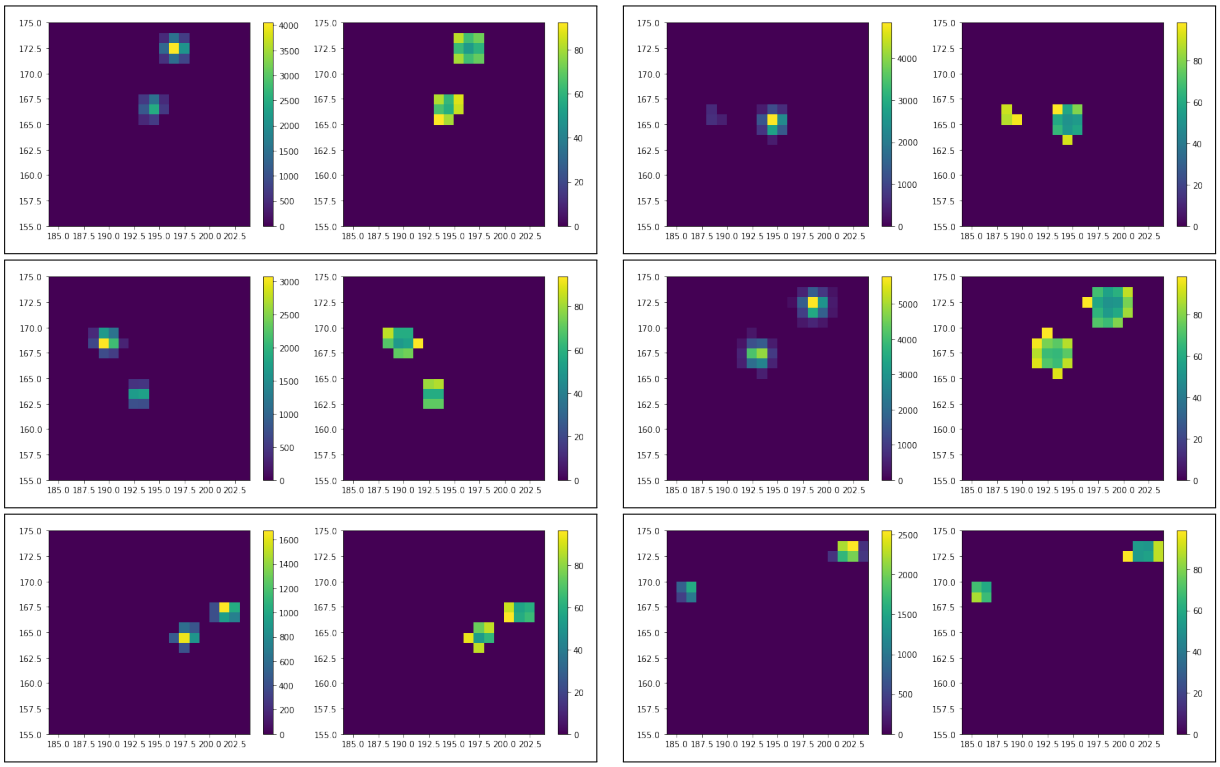


Figure 8. Six examples of two clusters in a single fiber (fiber 2) separated by less than 100 ns. The hits are shown as boxed pairs of heatmaps in ToT representation (left graph in the boxed pair of graphs) and ToA representation (right graph).

Figure 9 shows the distribution of distances between the photon pairs coming out of the same fiber where the photons are separated in time by less than 25 ns. Two distributions correspond to two different fibers. One can see that one distribution is slightly wider than the other, in agreement with a broader distribution for the more defocused beam from the fiber in the right part of Figure 5.

6. Theory: SPDC bi-spectrum and Hong-Ou-Mandel effect

The exact shape of the "HOM dip" feature illustrated in Fig. 1 depends on the spectrum (actually, the bi-spectrum) of the SPDC-produced daughter photons. In general, we expect the width δT of the dip as a function of delay time to scale inversely with the bandwidth $\delta\omega$ of the photons, i.e. $\delta T \sim \hbar/\delta\omega$. With a model of the down-conversion process we can calculate the exact bi-spectrum of the two-photon state, and then in turn predict a functional form for the shape of the HOM dip we observe.

In the SPDC source photon pairs are produced in two BBO crystals with optical axes orthogonal to each other, and as mentioned above the polarization of each photon is fixed with polarizers just before the coupling into single modes of polarization-maintaining fibers. This leaves only the temporal/frequency

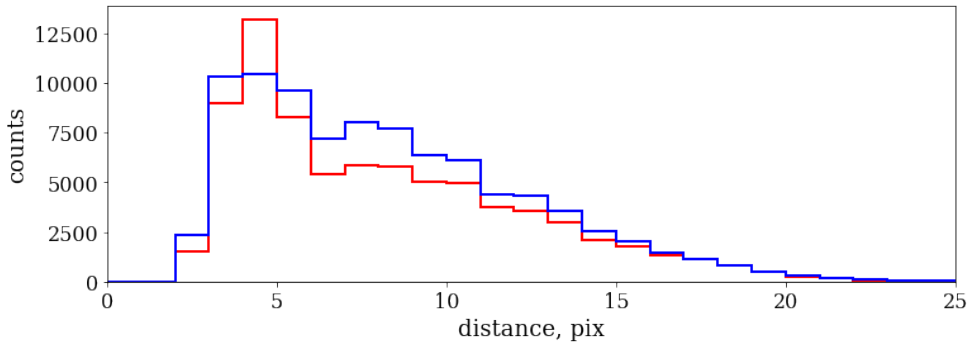


Figure 9. Distribution of distances between the photon pairs in the same fiber for fiber 1 (red) and fiber 2 (blue).

degrees of freedom, and one can write the full bi-photon state (for comprehensive details we recommend [46]) as follows:

$$|\Psi\rangle_{\text{SPDC}} = N\left(|\text{vac}\rangle + \eta \int d\omega_s d\omega_i \Psi\left(\omega_s, \omega_i\right)|\omega_s, \omega_i\rangle\right), \tag{1}$$

where N is the normalization constant, $|\text{vac}\rangle$ denotes a vacuum state of electromagnetic field, and the square of η is probability of one pump photon to down convert into two photons (typically η^2 is of the order of 10^{-8} for beams of this power). Here $\Psi\left(\omega_1, \omega_2\right)$ is a bi-photon wave-function over frequency, which determines the interference properties of the HOM effect. Noting that the subscripts s, i, p refer to "signal", "idler" and "pump" photons respectively, the wave-function in our case can be written as follows [46,47]:

$$\begin{aligned}\Psi\left(\omega_s, \omega_i\right) &= \frac{A_p}{\sqrt{2\pi\Delta\omega_p^2}} e^{-\frac{\left(\omega_p-\omega_i-\omega_s\right)^2}{2\Delta\omega_p^2}} e^{-\frac{iL\Delta k_z}{2}} \operatorname{sinc}\left(\frac{L\Delta k_z}{2}\right) \\ &\approx A_p \delta\left(\omega_p - \omega_i - \omega_s\right) e^{-\frac{iL\Delta k_z}{2}} \operatorname{sinc}\left(\frac{L\Delta k_z}{2}\right),\end{aligned} \tag{2}$$

where A_p is a pump amplitude, the function $\operatorname{sinc}(x) = \frac{\sin x}{x}$, and L is the length of crystals. Here $\vec{k}$ is a photon wavevector and k_z is its component along the pump beam axis; then $\Delta k_z = k_{pz}\left(\omega_p, \phi_0\right) - k_{sz}\left(\omega_s, \theta_s\right) - k_{iz}\left(\omega_i, \theta_i\right)$ is a phase mismatch. Here the components of wave vectors (k_{pz}, k_{iz}, k_{sz}) depend on the pump, signal and idler frequencies $(\omega_p, \omega_s, \omega_i)$; crystal indices of refraction; direction of propagation (θ_s,θ_i); optical axis orientation ϕ_0 and syncronism type. A detailed account of this derivation can be found in [46].

The first line of Eq. 2 depends on the bandwidth $\Delta\omega_p$ of the pump beam. But for our source this is very narrow (less than 1 nm linewidth) compared to the width of the SPDC spectrum, and so we can replace the Gaussian with a Dirac delta function, that effectively fixes the sum of the energies of the two daughters. It is worth mentioning that all optical elements downstream of the source have wide enough frequency band-pass to not limit the SPDC spectrum. Fibers have a specific refraction index (dispersion) profile, but in fact fibers dispersion should not significantly affect observation of HOM interference due to the dispersion cancellation effect [48–50] as long as we assume that the refraction index profile and length of fibers 1 and 2 do not vary too much.

The SPDC source produces photon pairs in near frequency degenerate regime: $\omega_s \approx \omega_i$, and $\omega_s + \omega_i = \omega_p$ leading to strong correlations between the two photons. To prove that reliable registration of photon pairs in the same fiber is feasible and that they are not due to some instrumental features, we performed a scan of the optical delay to observe the HOM effect. The scan was done by incrementing the spatial separation between the two fiber couplers in one of the optical paths before the beam splitter as shown in Figure 4. In accordance with (1) and (2) the two-photon coincidence rate between the two fibers (HOM dip) and the rates in each single fiber 1 and 2 (the two-photon intensity correlation or bunching) can be described by the following expressions:

$$\begin{aligned} N_{\text{HOM dip}} &= N_{(|d|\gg d_0)} \left(T^4 + R^4 - 2T^2R^2 f(d-d_0) \right) \\ N_{\text{fib. 1,2}} &= N_{(|d|\gg d_0)} (TR)^2 \left(1 + f(d-d_0)\right), \end{aligned} \tag{3}$$

where the beam splitter transmittance and reflectance are $T^2 + R^2 = 1$, d is delay length, and d_0 is delay at the HOM dip center. In case of narrow-band pump the function $f(d-d_0)$ reads [46]:

$$f(d-d_0) = \frac{3}{4\sqrt{\pi}} \int dy \, [\text{sinc}\left(y^2\right)]^2 \, e^{-iy\frac{\sqrt{4\log 2}(d-d0)}{\text{FWHM}}}, \tag{4}$$

where $\text{FWHM} = \sqrt{2\pi \log 2} c/\Delta\omega_{\text{SPDC}}$ is the the full width half maximum for both the HOM dip and the coincidence rates in each single fiber, 1 and 2; and c is the speed of light. Here $\Delta\omega_{\text{SPDC}}$ is the SPDC spectrum width (and thus $\Delta\lambda_{\text{SPDC}} = (8\pi c/\omega_{\text{p}}^2)\Delta\omega_{\text{SPDC}}$). The experimental data is described with equations (3) and (4), where we determined from the fit the number of coincidences, $N_{(|d|\gg d_0)}$; coefficients T and R; HOM dip position d_0 and FWHM.

7. Results

To analyse the data as function of the delay between two photons we binned the dataset according to the distance traveled by the adjustable fiber coupler. For each distance bin we determine the number of signal events in the time difference distributions by fitting them with the same functions as in Figure 7. Note that the random coincidences are automatically taken into account by the fitting procedure. Figure 10 shows the number of coincidences between two different fibers for the experimental data and the corresponding fit as function of the delay. The HOM dip is obvious around the delay value of 0.18 mm. One can see that the data is in agreement with theoretical model and, in general, with expectations described in the literature [46,51].

The same datasets were used to study behaviour of the photon bunching (coincidence rate of photons in the same fiber) as function of the delay. The results are shown in the same Figure 10 for two different fibers used in the experiment. Spikes in the coincidence rates with similar width and at the same delay values as for the HOM dip are clearly visible, confirming that the detected photon pairs are real.

The FWHM of the dip is 8.2 micron or 27 fs, which is consistent with the bandwidth of the SPDC source of about 40 nm. The visibility is $42 \pm 3\%$. The non-ideal visibility can be caused by slightly different wavelength of the two photons due to different selection in the corresponding fiber couplers in the SPDC source and their slightly different polarization since the final 1 m long run of the fibers before the camera was not polarization preserving.

The coincidence rates in single fibers and between two different fibers should be in the proportion 1:1:2 if they are measured away from the HOM dip, so for non-interfering, distinguishable photons. This is a simple combinatorial property of the 50:50 beam splitter, which is also consistent with Equation (3) above.

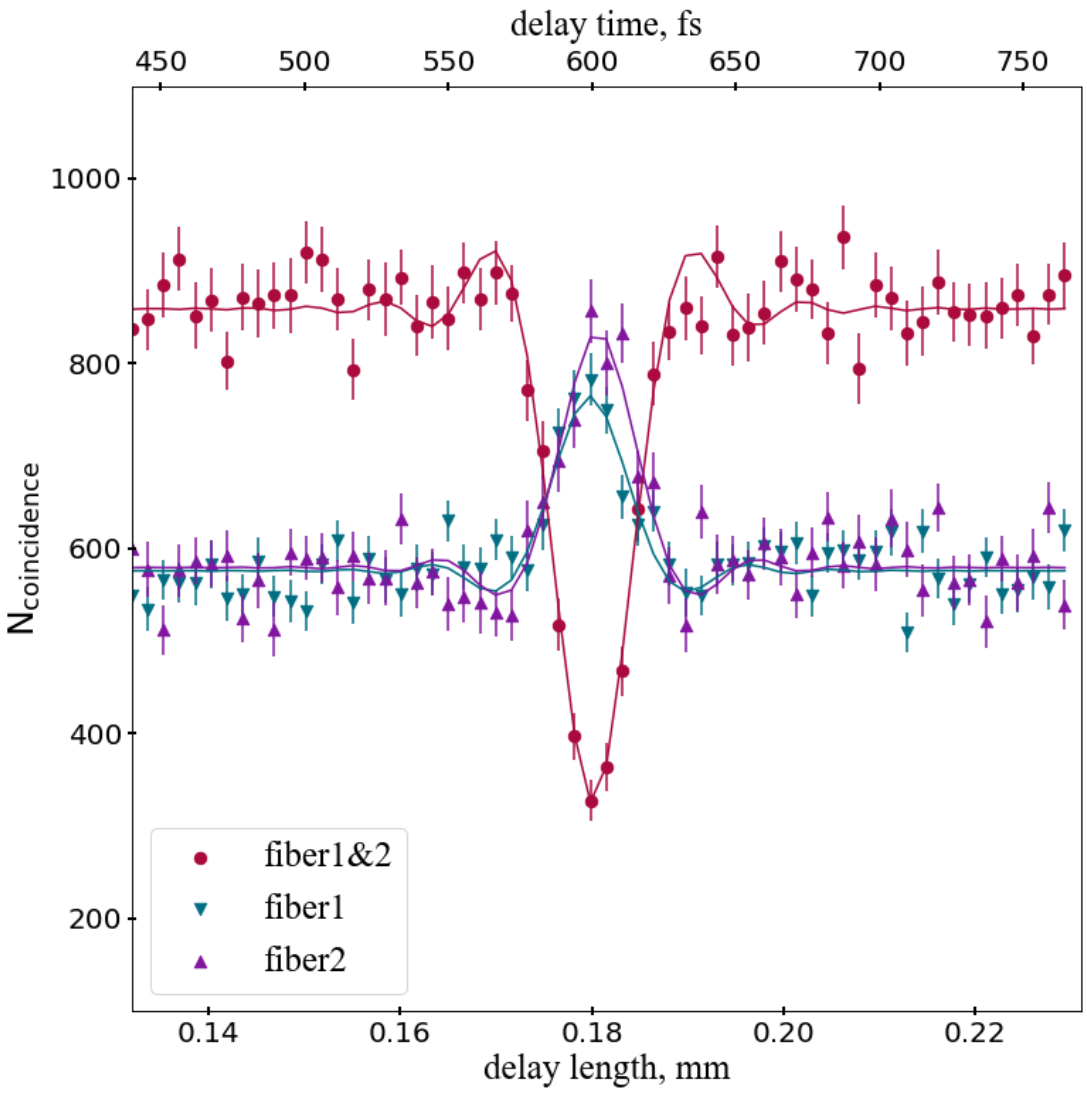


Figure 10. Number of coincidences between two different fibers (fiber 1&2) and within the same fibers (fiber 1, fiber 2), shown for experimental data and corresponding fits as function of the delay between two photons. The delay is expressed in mm (bottom horizontal scale) and in fs (top horizontal scale). The HOM dip is obvious around the delay value of 0.18 mm.

However, the three rates shown in Figure 10 do not follow this proportion. The reason is a systematic effect in the intensifier due to the MCP afterpulsing. Electron avalanches in MCP could result in secondary electrons or ions producing independent hits in the vicinity of the primary hit [52,53]. The time difference between the main hit and afterpulse hit is small, typically of the order of nanoseconds or less, so the coincidence finding algorithm would identify some of these cases as pairs of photons. This will constitute an important systematic background for our measurements.

The probability of finding a fake single fiber coincidence due to this effect was determined from the data. Assuming that the produced quantum state has only one pair of photons (so neglecting multi-pair

production in the SPDC source) we selected a pure sample of registered photon pairs in two different fibers using events in the coincidence peak in Figure 7. Then, for this sample, we required a companion hit in the same fiber, for either of the two fibers, using the same pair finding algorithm as used in the analysis. We found, on average, 153 pairs in a single fiber separated in time by less than 50 ns whilst the number of coincidences between the two separate fibers was 82390. Therefore, the afterpulsing probability in our conditions is 0.19%. Multiplying it by the number of single photon hits per fiber, about 10M in the full dataset, and taking into account the bin width in Figure 10 we estimate the instrumental background of approximately 85 for the single fiber coincidence rates. After subtraction of this value from the number of coincidences in Figure 10 the ratio of the three rates agrees with the 1:1:2 proportion within uncertainties. We also measured the afterpulsing probability using an independent dataset without the beam splitter with the result in agreement with the above estimation. We note that this correction affects only negligibly the HOM dip and corresponding peaks for the coincidences since the change of the coincidence rates is very small, 0.19%.

Figure 11 shows the sum of two-photon coincidence rates in single fibers and between two fibers as function of the delay. As expected the total rate is constant as required by unitarity and does not show dependence on the delay within errors. It also confirms that there are no visible inefficiencies or other systematic effects in the methodology to find photon coincidences in a single fiber.

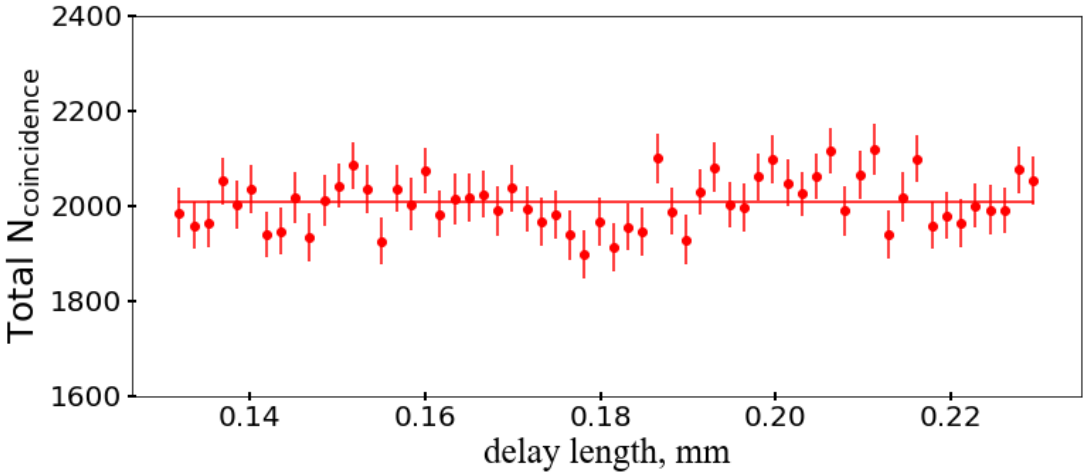


Figure 11. Sum of two-photon coincidence rates in single fibers and between two fibers as function of the delay.

8. Discussion and Conclusions

Using the HOM effect we demonstrated that the fast time-stamping camera can be employed to efficiently count small number of photons in fibers if the outgoing photons are spread enough spatially in the camera. As we already mentioned there are several important experimental parameters which could affect this photon counting technique: the photon footprint in the sensor, size of the illuminated spot, pixel deadtime and time resolution. Let us consider limitations stemming from the Tpx3Cam parameters.

Using average cluster size of $3 \times 3 = 9$ pixels and the fiber spot size of 15 pixels in diameter (so with total area of about 177 pixels) we can estimate that the probability of two simultaneous photons to blend is about 10%. This makes it clear that the technique has a limited dynamic range since the blending

would depend strongly on the number of photons. Of course, this source of inefficiency would need to be convoluted with the intensifier quantum efficiency, of the order of 30-35%, which would be another limiting factor for the larger number of photons detected in coincidence.

The pixel deadtime is about 1 microsecond. This limits the rate in the fiber to 10^6 photons/sec allowing for about 5% inefficiency assuming a CW photon source. This value is orders of magnitude larger than rates in the presented experiments. The total data acquisition bandwidth of the readout is about 10^7 photons/sec. The time resolution is a few nanoseconds, so the photons from different pulses should be separated by more than few dozen nanoseconds so as not to cause problems for the clustering algorithm. The previous rate limitation will be reached sooner than this one.

The expected HOM dip in the two fiber coincidences and spikes in the single fiber coincidence rates are in agreement with expectations as well as their sum proving that the above effects are under control for distinguishing single photon and double photon cases. Though this is consistent with no effect within uncertainties, we note that a slightly lower amplitude of the "fiber 1" peak in Figure 10 and a downward fluctuation around the center of the HOM dip in Figure 11 may indicate influence of the hit blending in fiber 1, which had narrower focusing.

In summary, we believe that this approach is simple, robust and can find applications in photon counting in situations when the number of photons in fibers is small. Also, it can be easily scaled to a large number of fibers or photon beams. We estimate that the camera parameters would allow the use of this technique for a grid of $100 = 10 \times 10$ bunched photon beams. Distribution of the beams in two dimensions could be achieved by employing acousto-optic modulators (AOM). AOMs are widely used, for example, for preparing and addressing Bell states and measuring the entanglement fidelity of the neutral atoms [54,55].

Author Contributions: A.N. conceptualized the experiment; A.N and M.K prepared and performed the measurements; all authors contributed to the data analysis and manuscript preparation.

Funding: This work was supported by the U.S. Department of Energy QuantISED award and by the grant LM2018109 of Ministry of Education, Youth and Sports as well as by Centre of Advanced Applied Sciences CZ.02.1.01/0.0/0.0/16-019/0000778, co-financed by the European Union.

Acknowledgments: We thank Henning Weier for helpful discussions.

Conflicts of Interest: The authors declare no conflict of interest.

Abbreviations

The following abbreviations are used in this manuscript:

MCP	micro-channel plate
QE	quantum efficiency
SPDC	spontaneous parametric down conversion
CW	continuous wave
PMF	polarization maintaining fiber
AOM	acousto-optic modulator

1. Ollivier, H.; Maillette de Buy Wenniger, I.; Thomas, S.; Wein, S.C.; Harouri, A.; Coppola, G.; Hilaire, P.; Millet, C.; Lemaître, A.; Sagnes, I.; Krebs, O.; Lanco, L.; Loredo, J.C.; Antón, C.; Somaschi, N.; Senellart, P. Reproducibility of High-Performance Quantum Dot Single-Photon Sources. *ACS Photonics* **2020**, *7*, 1050–1059, [https://doi.org/10.1021/acsphotonics.9b01805]. doi:10.1021/acsphotonics.9b01805.
2. Saffman, M.; Walker, T.G. Creating single-atom and single-photon sources from entangled atomic ensembles. *Phys. Rev. A* **2002**, *66*, 065403. doi:10.1103/PhysRevA.66.065403.

3. Firstenberg, O.; Adams, C.S.; Hofferberth, S. Nonlinear quantum optics mediated by Rydberg interactions. *Journal of Physics B: Atomic, Molecular and Optical Physics* **2016**, *49*, 152003. doi:10.1088/0953-4075/49/15/152003.
4. Ma, L.; Tang, X.; Slattery, O.T. Optical quantum memory and its applications in quantum communication systems. *J Res Natl Inst Stan* **2020**.
5. Scriminich, A.; Namazi, M.; Flament, M.; Gera, S.; Sagona-Stophel, S.; Vallone, G.; Villoresi, P.; Figueroa, E. Hong-Ou-Mandel interference between two weak coherent pulses retrieved from room-temperature quantum memories. Quantum Information and Measurement (QIM) V: Quantum Technologies. Optical Society of America, 2019, p. T5A.70. doi:10.1364/QIM.2019.T5A.70.
6. Chen, Y.A.; Chen, S.; Yuan, Z.S.; Zhao, B.; Chuu, C.S.; Schmiedmayer, J.; Pan, J.W. Memory-built-in quantum teleportation with photonic and atomic qubits. *Nature Physics* **2008**, *4*, 103–107. doi:10.1038/nphys832.
7. Motes, K.R.; Olson, J.P.; Rabeaux, E.J.; Dowling, J.P.; Olson, S.J.; Rohde, P.P. Linear Optical Quantum Metrology with Single Photons: Exploiting Spontaneously Generated Entanglement to Beat the Shot-Noise Limit. *Phys. Rev. Lett.* **2015**, *114*, 170802. doi:10.1103/PhysRevLett.114.170802.
8. Jeffrey, E.; Peters, N.A.; Kwiat, P.G. Towards a periodic deterministic source of arbitrary single-photon states. *New Journal of Physics* **2004**, *6*, 100–100. doi:10.1088/1367-2630/6/1/100.
9. Ramelow, S.; Mech, A.; Giustina, M.; Gröblacher, S.; Wieczorek, W.; Beyer, J.; Lita, A.; Calkins, B.; Gerrits, T.; Nam, S.W.; Zeilinger, A.; Ursin, R. Highly efficient heralding of entangled single photons. *Opt. Express* **2013**, *21*, 6707–6717. doi:10.1364/OE.21.006707.
10. Hong, C.K.; Ou, Z.Y.; Mandel, L. Measurement of subpicosecond time intervals between two photons by interference. *Phys. Rev. Lett.* **1987**, *59*, 2044–2046. doi:10.1103/PhysRevLett.59.2044.
11. Hadfield, R.H. Single-photon detectors for optical quantum information applications. *Nature Photonics* **2009**, *3*, 696–705. doi:10.1038/nphoton.2009.230.
12. Seitz, P.; Theuwissen, A.J., Eds. *Single-Photon Imaging*; Springer Berlin Heidelberg, 2011. doi:10.1007/978-3-642-18443-7.
13. Migdall, A.; Polyakov, S.V.; Fan, J.; Bienfang, J.C., Eds. *Single-Photon Generation and Detection*; Vol. 45, *Experimental Methods in the Physical Sciences*, Academic Press, 2013. doi:https://doi.org/10.1016/B978-0-12-387695-9.00016-0.
14. Zhang, L.; Neves, L.; Lundeen, J.S.; Walmsley, I.A. A characterization of the single-photon sensitivity of an electron multiplying charge-coupled device. *Journal of Physics B: Atomic, Molecular and Optical Physics* **2009**, *42*, 114011. doi:10.1088/0953-4075/42/11/114011.
15. Avella, A.; Ruo-Berchera, I.; Degiovanni, I.P.; Brida, G.; Genovese, M. Absolute calibration of an EMCCD camera by quantum correlation, linking photon counting to the analog regime. *Optics Letters* **2016**, *41*, 1841. doi:10.1364/ol.41.001841.
16. Moreau, P.A.; Toninelli, E.; Gregory, T.; Padgett, M.J. Imaging with quantum states of light. *Nature Reviews Physics* **2019**, *1*, 367–380. doi:10.1038/s42254-019-0056-0.
17. Gasparini, L.; Bessire, B.; Unternährer, M.; Stefanov, A.; Boiko, D.; Perenzoni, M.; Stoppa, D. SUPERTWIN: towards 100kpixel CMOS quantum image sensors for quantum optics applications. Quantum Sensing and Nano Electronics and Photonics XIV; Razeghi, M., Ed. SPIE, 2017. doi:10.1117/12.2253598.
18. Perenzoni, M.; Pancheri, L.; Stoppa, D. Compact SPAD-Based Pixel Architectures for Time-Resolved Image Sensors. *Sensors* **2016**, *16*. doi:10.3390/s16050745.
19. Lee, M.J.; Charbon, E. Progress in single-photon avalanche diode image sensors in standard CMOS: From two-dimensional monolithic to three-dimensional-stacked technology. *Japanese Journal of Applied Physics* **2018**, *57*, 1002A3. doi:10.7567/jjap.57.1002a3.
20. Jiang, L.A.; Dauler, E.A.; Chang, J.T. Photon-number-resolving detector with 10 bits of resolution. *Phys. Rev. A* **2007**, *75*, 062325. doi:10.1103/PhysRevA.75.062325.
21. Morimoto, K.; Ardelean, A.; Wu, M.L.; Ulku, A.C.; Antolovic, I.M.; Bruschini, C.; Charbon, E. Megapixel time-gated SPAD image sensor for 2D and 3D imaging applications. *Optica* **2020**, *7*, 346. doi:10.1364/optica.386574.

22. Brida, G.; Caspani, L.; Gatti, A.; Genovese, M.; Meda, A.; Berchera, I.R. Measurement of Sub-Shot-Noise Spatial Correlations without Background Subtraction. *Phys. Rev. Lett.* **2009**, *102*, 213602. doi:10.1103/PhysRevLett.102.213602.
23. Brida, G.; Degiovanni, I.P.; Florio, A.; Genovese, M.; Giorda, P.; Meda, A.; Paris, M.G.A.; Shurupov, A. Experimental Estimation of Entanglement at the Quantum Limit. *Phys. Rev. Lett.* **2010**, *104*, 100501. doi:10.1103/PhysRevLett.104.100501.
24. Reichert, M.; Sun, X.; Fleischer, J.W. Quality of spatial entanglement propagation. *Phys. Rev. A* **2017**, *95*, 063836. doi:10.1103/PhysRevA.95.063836.
25. Jost, B.M.; Sergienko, A.V.; Abouraddy, A.F.; Saleh, B.E.A.; Teich, M.C. Spatial correlations of spontaneously down-converted photon pairs detected with a single-photon-sensitive CCD camera. *Opt. Express* **1998**, *3*, 81–88. doi:10.1364/OE.3.000081.
26. Jachura, M.; Chrapkiewicz, R. Shot-by-shot imaging of Hong–Ou–Mandel interference with an intensified sCMOS camera. *Opt. Lett.* **2015**, *40*, 1540–1543. doi:10.1364/OL.40.001540.
27. Fickler, R.; Krenn, M.; Lapkiewicz, R.; Ramelow, S.; Zeilinger, A. Real-Time Imaging of Quantum Entanglement. *Scientific Reports* **2013**, *3*, 1914.
28. Just, F.; Filipenko, M.; Cavanna, A.; Michel, T.; Gleixner, T.; Taheri, M.; Vallerga, J.; Campbell, M.; Tick, T.; Anton, G.; Chekhova, M.V.; Leuchs, G. Detection of non-classical space-time correlations with a novel type of single-photon camera. *Opt. Express* **2014**, *22*, 17561–17572. doi:10.1364/OE.22.017561.
29. Divochiy, A.; Marsili, F.; Bitauld, D.; Gaggero, A.; Leoni, R.; Mattioli, F.; Korneev, A.; Seleznev, V.; Kaurova, N.; Minaeva, O.; Gol'tsman, G.; Lagoudakis, K.G.; Benkhaoul, M.; Lévy, F.; Fiore, A. Superconducting nanowire photon-number-resolving detector at telecommunication wavelengths. *Nature Photonics* **2008**, *2*, 302–306. doi:10.1038/nphoton.2008.51.
30. Zhu, D.; Colangelo, M.; Chen, C.; Korzh, B.A.; Wong, F.N.C.; Shaw, M.D.; Berggren, K.K. Resolving Photon Numbers Using a Superconducting Nanowire with Impedance-Matching Taper. *Nano Letters* **2020**. doi:10.1021/acs.nanolett.0c00985.
31. Korzh, B.; Zhao, Q.Y.; Allmaras, J.P.; Frasca, S.; Autry, T.M.; Bersin, E.A.; Beyer, A.D.; Briggs, R.M.; Bumble, B.; Colangelo, M.; Crouch, G.M.; Dane, A.E.; Gerrits, T.; Lita, A.E.; Marsili, F.; Moody, G.; Peña, C.; Ramirez, E.; Rezac, J.D.; Sinclair, N.; Stevens, M.J.; Velasco, A.E.; Verma, V.B.; Wollman, E.E.; Xie, S.; Zhu, D.; Hale, P.D.; Spiropulu, M.; Silverman, K.L.; Mirin, R.P.; Nam, S.W.; Kozorezov, A.G.; Shaw, M.D.; Berggren, K.K. Demonstration of sub-3 ps temporal resolution with a superconducting nanowire single-photon detector. *Nature Photonics* **2020**, *14*, 250–255. doi:10.1038/s41566-020-0589-x.
32. Cabrera, B.; Clarke, R.M.; Colling, P.; Miller, A.J.; Nam, S.; Romani, R.W. Detection of single infrared, optical, and ultraviolet photons using superconducting transition edge sensors. *Applied Physics Letters* **1998**, *73*, 735–737. doi:10.1063/1.121984.
33. Lita, A.E.; Miller, A.J.; Nam, S.W. Counting near-infrared single-photons with 95% efficiency. *Optics Express* **2008**, *16*, 3032. doi:10.1364/oe.16.003032.
34. Kok, P.; Munro, W.J.; Nemoto, K.; Ralph, T.C.; Dowling, J.P.; Milburn, G.J. Linear optical quantum computing with photonic qubits. *Rev. Mod. Phys.* **2007**, *79*, 135–174. doi:10.1103/RevModPhys.79.135.
35. O'Brien, J.L. Optical Quantum Computing. *Science* **2007**, *318*, 1567–1570. doi:10.1126/science.1142892.
36. Fisher-Levine, M.; Nomerotski, A. TimepixCam: a fast optical imager with time-stamping. *Journal of Instrumentation* **2016**, *11*, C03016.
37. Zhao, A.; others. Coincidence velocity map imaging using Tpx3Cam, a time stamping optical camera with 1.5 ns timing resolution. *Review of Scientific Instruments* **2017**, *88*, 113104. doi:10.1063/1.4996888.
38. Nomerotski, A.; Chakaberia, I.; Fisher-Levine, M.; Janoska, Z.; Takacs, P.; Tsang, T. Characterization of TimepixCam, a fast imager for the time-stamping of optical photons. *Journal of Instrumentation* **2017**, *12*, C01017.
39. Poikela, T.; others. Timepix3: a 65K channel hybrid pixel readout chip with simultaneous ToA/ToT and sparse readout. *Journal of instrumentation* **2014**, *9*, C05013.

40. Ianzano, C.; Svihra, P.; Flament, M.; Hardy, A.; Cui, G.; Nomerotski, A.; Figueroa, E. Fast camera spatial characterization of photonic polarization entanglement. *Scientific Reports* **2020**, *10*. doi:10.1038/s41598-020-62020-z.
41. Nomerotski, A.; Katramatos, D.; Stankus, P.; Svihra, P.; Cui, G.; Gera, S.; Flament, M.; Figueroa, E. Spatial and temporal characterization of polarization entanglement. *International Journal of Quantum Information* **2020**, *18*, 1941027. doi:10.1142/s0219749919410272.
42. Zhang, Y.; England, D.; Nomerotski, A.; Svihra, P.; Ferrante, S.; Hockett, P.; Sussman, B. Multidimensional quantum-enhanced target detection via spectrotemporal-correlation measurements. *Phys. Rev. A* **2020**, *101*, 053808. doi:10.1103/PhysRevA.101.053808.
43. Sen, R.; Hirvonen, L.M.; Zhdanov, A.; Svihra, P.; Andersson-Engels, S.; Nomerotski, A.; Papkovsky, D. New luminescence lifetime macro-imager based on a Tpx3Cam optical camera. *Biomed. Opt. Express* **2020**, *11*, 77–88. doi:10.1364/BOE.11.000077.
44. Turecek, D.; Jakubek, J.; Soukup, P. USB 3.0 readout and time-walk correction method for Timepix3 detector. *Journal of Instrumentation* **2016**, *11*, C12065–C12065. doi:10.1088/1748-0221/11/12/c12065.
45. Ianzano, C.; Svihra, P.; Flament, M.; Hardy, A.; Cui, G.; Nomerotski, A.; Figueroa, E. Spatial characterization of photonic polarization entanglement using a fast camera. *arXiv:1808.06720* **2018**.
46. Ou, Z.Y.J. *Multi-photon quantum interference*; Vol. 43, Springer, 2007.
47. Cialdi, S.; Castelli, F.; Paris, M.G. Properties of entangled photon pairs generated by a CW laser with small coherence time: theory and experiment. *Journal of Modern Optics* **2009**, *56*, 215–225, [https://doi.org/10.1080/09500340802187332]. doi:10.1080/09500340802187332.
48. Franson, J.D. Nonlocal cancellation of dispersion. *Phys. Rev. A* **1992**, *45*, 3126–3132. doi:10.1103/PhysRevA.45.3126.
49. Steinberg, A.M.; Kwiat, P.G.; Chiao, R.Y. Dispersion cancellation and high-resolution time measurements in a fourth-order optical interferometer. *Phys. Rev. A* **1992**, *45*, 6659–6665. doi:10.1103/PhysRevA.45.6659.
50. Steinberg, A.M.; Kwiat, P.G.; Chiao, R.Y. Dispersion cancellation in a measurement of the single-photon propagation velocity in glass. *Phys. Rev. Lett.* **1992**, *68*, 2421–2424. doi:10.1103/PhysRevLett.68.2421.
51. Rarity, J.G.; Tapster, P.R. Fourth-order interference in parametric downconversion. *J. Opt. Soc. Am. B* **1989**, *6*, 1221–1226. doi:10.1364/JOSAB.6.001221.
52. Orlov, D.; Ruardij, T.; Pinto, S.D.; Glazenborg, R.; Kernen, E. High collection efficiency MCPs for photon counting detectors. *Journal of Instrumentation* **2018**, *13*, C01047–C01047. doi:10.1088/1748-0221/13/01/c01047.
53. Orlov, D.A.; Glazenborg, R.; Ortega, R.; Kernen, E. UV/visible high-sensitivity MCP-PMT single-photon GHz counting detector for long-range lidar instrumentations. *CEAS Space Journal* **2019**, *11*, 405–411. doi:10.1007/s12567-019-00260-0.
54. Xia, T.; Lichtman, M.; Maller, K.; Carr, A.W.; Piotrowicz, M.J.; Isenhower, L.; Saffman, M. Randomized Benchmarking of Single-Qubit Gates in a 2D Array of Neutral-Atom Qubits. *Phys. Rev. Lett.* **2015**, *114*, 100503. doi:10.1103/PhysRevLett.114.100503.
55. Graham, T.M.; Kwon, M.; Grinkemeyer, B.; Marra, Z.; Jiang, X.; Lichtman, M.T.; Sun, Y.; Ebert, M.; Saffman, M. Rydberg-Mediated Entanglement in a Two-Dimensional Neutral Atom Qubit Array. *Phys. Rev. Lett.* **2019**, *123*, 230501. doi:10.1103/PhysRevLett.123.230501.